ADVANCED FUNCTIONAL MATERIALS
www.afm-journal.de

The Multiphasic Teeth of *Chiton Articulatus*, an Abrasion-Resistant and Self-Sharpening Tool for Hard Algae Collection

*Devis Montroni, Ezra Sarmiento, Ruoheng Zhao, Phani Saketh Dasika, John Michael Connolly, Richard Wuhrer, Yugang Zhang, Mikhail Zhernenkov, Taifeng Wang, Brenda Paola Ramirez-Santana, Leigh Sheppard, Omar Hernando Avila-Poveda, Atsushi Arakaki, Michiko Nemoto, Pablo Zavattieri, and David Kisailus**

Chiton articulatus **is a species of mollusk living in the tropical Pacific intertidal rocky shores of Mexico. This species feeds on solid waste organic sources, including hard crustose algae that grow on rocky substrates, by grazing on them with its radula, a flexible chitinous membrane lined with mineralized major lateral teeth. In this study, the composition, morphology, and resulting mechanics of the mature teeth of this species, which have yet to be examined, are revealed. The results show the presence of multiphasic mature teeth, each consisting of aligned hard magnetite nanoparticles on the leading edge of the tooth underneath which are magnetite lamellae, followed by goethite, lepidocrocite, and eventually hydroxyapatite near the trailing edge. This multiregional structure demonstrates a gradation in hardness as well as different microstructural features integrated with tough interfaces. The combination of these microstructural and phase arrangements results in an abrasion-resistant tough structure with a self-sharpening ability. The results of this work will help contribute to developing new bioinspired designs while also helping to understand the evolution and feeding habits of these intriguing invertebrates.**

1. Introduction

Natural materials have generated significant interest from the scientific community due to their remarkable properties that are derived from inherently weak individual components. In fact, nature has been able, through millions of years of evolution, to develop efficient strategies for the synthesis of multiscale structures from a surprisingly limited set of constituent materials.[1–3] These constituents are often organized in a precise, hierarchical structure that maximizes their potential properties. Many different studies have been successfully carried out in order to understand these systems,[4–7] and have led to the reproduction of analog, or biomimetic, structures to exploit this knowledge for a variety of technological applications.[8–15] Biomineralizing organisms have evolved structures (i.e., shells, teeth, or skeletons)

D. Montroni, E. Sarmiento, R. Zhao, T. Wang, D. Kisailus
Department of Materials Science and Engineering
University of California at Irvine
Irvine, CA 92697, USA
E-mail: david.k@uci.edu

D. Montroni
Department of Chemistry "G. Ciamician"
Alma Mater Studiorum – Università di Bologna
Bologna 40126, Italy

The ORCID identification number(s) for the author(s) of this article can be found under https://doi.org/10.1002/adfm.202401658

DOI: 10.1002/adfm.202401658

P. S. Dasika, J. M. Connolly, P. Zavattieri
Lyles School of Civil Engineering
Purdue University
West Lafayette, IN 47907, USA

R. Wuhrer
Advanced Materials Characterization Facility
Western Sydney University
Locked Bag 1797, Penrith, NSW 2751, Australia

Y. Zhang, M. Zhernenkov
National Synchrotron Light Source II
Brookhaven National Laboratory
Upton, NY 11973, USA

B. P. Ramirez-Santana, O. H. Avila-Poveda
Facultad de Ciencias del Mar (FACIMAR)
Universidad Autonoma de Sinaloa (UAS)
Mazatlan, Sinaloa 82190, Mexico

B. P. Ramirez-Santana, O. H. Avila-Poveda
Proyecto Quitón del Pacífico tropical mexicano
Mazatlán, Sinaloa 82190, México

that are adapted to mitigate predation and environmental stresses, or provide predatory advantages.[16–27] Investigations of these structures have revealed surprising properties, particularly for their mechanical strength and toughness.[3,28] Among the many systems studied, chiton teeth show great potential and promise for developing advanced novel materials.[29–34]

Chitons are mollusks dorsoventrally flattened and show, from a top view perspective, an elliptic oval body shape and a shell, or sclerotome, which consists of eight overlapping plates.[35,36] Like most other groups of mollusks, the chiton feeds using a radula, a belt-like structure with transversal rows of teeth attached to it via a flexible organic structure (stylus). This organ is located in the buccal cavity (analogous to the human mouth) and is used to graze food particles (a schematic is depicted in **Figure 1**A).[37–39] The composition and morphology of the radular teeth vary among chitons[29–31,40–47] with differences primarily related to their diet and ecology.[48,49] Generally in these invertebrates, the radula is used to graze on a substrate, usually rocks, to collect food particles of various organic origin (Figure 1B,C). In a radula, only a few rows of teeth are actually involved in the grazing process[5] and, as a result of the intense stresses during the feeding of some species, teeth have been observed to wear down.[30,50] For this reason, a continuous supply of new rows of teeth steadily enters the wearing zone while teeth at the end of the radular belt break loose at the same rate.[30,51] This biomineralization occurs at a rate dependent on the season, ranging between 2 and 17 teeth per month through an estimated longevity of ≈57 months, corresponding with a *C. articulatus* specimen of 77 mm total length.[52–54]

There are fifty-nine species of chitons reported so far in the Pacific and Atlantic waters of Mexico.[55,56] Among them, *Chiton articulatus* (Figure 1D) is the largest, most abundant, and most frequently observed species exclusively in the rocky intertidal,[57–59] allowing it to support a commercial harvest for alimentary purposes.[60,61] It is endemic to the Mexican Tropical Pacific, occurring from Oaxaca (16° N) to Sinaloa (23° N), as illustrated in Figure 1E.[56,62] It is a species that only inhabits intertidal rocky shores and demonstrates a wide ecological niche as omnivorous or detritivorous, thus acting as both a decomposer and nutrient recycler.[54] This chiton feeds on waste solid derived from the decomposition of organic sources (detritus), as well as various sources of algae, including hard mineralized crustose algae (Figure 1F,G).[63] This is different from other well-studied species, such as *Cryptochiton stelleri*, which feed on softer substrates. As such, *C. articulatus* is challenged with grazing, breaking, and detaching the algae colony from hard substrates upon which it grows. To achieve this, the teeth must be sufficiently hard and tough to abrade the rock, providing significant impetus to investigate this intriguing material for its abrasion-resistant properties.

Thus, this study will focus on the overall compositional, morphological, and mechanical characterization of the major lateral teeth of *C. articulatus*. The results will help unravel how these teeth are able to withstand high stresses during mastication on hard surfaces. Understanding of this unique structure may help unveil important features for the design of future biomimetic and bioinspired hard abrasion-resistant materials and structures.

2. Results

2.1. Phase Characterization

A radula collected by dissection of the animal appears as a membrane equipped with multiple rows of teeth (Figure 1H). In each row, two primary lateral teeth, which appear darker, are present (Figure 1I,J) and protrude perpendicular from the flat plane of the radular belt. As these lateral teeth are most involved in the interactions with the rocky surfaces upon which the animal grazes, they are the focus of this study. Isolation of the tooth from the radular belt and subsequent examination by SEM (Figure 1K) reveals the presence of two different components: i) a curved and pointed mineralized tooth and ii) a cylinder-like arm (stylus) that connects the tooth to the radular membrane.[34]

In the radula of most chiton species, the teeth can be found at different maturation stages depending on their location along the membrane.[26] In this work, we will refer to "tooth" as either a fully mature (i.e., completely mineralized) tooth that can be found in the active region of the radula, or one found in a row preceding that region (also fully mature) but has not yet been subjected to abrasion on rocky surfaces.

Observation of a polished longitudinal section of a tooth (Figure 1L) using optical microscopy revealed three different regions. "Region 1" is located on the leading edge of the tooth and can be seen as a dark region covering the entire edge. An off-white colored "Region 3" is located on the trailing edge of the tooth and covers most of the area of the tooth section. Between these two regions and located within the top half of the tooth, is a transition region ("Region 2") with a brownish-orange coloration.

Similarly, a longitudinal section of a tooth was observed using backscattered SEM (**Figure 2**). The micrograph shows that each of the three regions has a distinct level of contrast and thus, energy dispersive spectroscopy (EDS) X-ray mapping (XRM) was used to evaluate specific elemental components and their location. Strong signals for Fe and O were observed in Regions 1 and 2, with a larger O/Fe ratio in Region 2. Region 3 showed a strong signal for Ca and P. Minor elements such as N, S, Mg, Na, Si, K, and Cl (Figure 2; Figure S1, Supporting Information) were

L. Sheppard
School of Engineering
Design and Built Environment
Western Sydney University
Locked Bag 1797, Penrith, NSW 2751, Australia
O. H. Avila-Poveda
Programa de Investigadoras e Investigadores por México
Consejo Nacional de Humanidades
Ciencias y Tecnologías (CONAHCyT)
Ciudad de México 03940, México
A. Arakaki
Division of Biotechnology and Life Science
Institute of Engineering
Tokyo University of Agriculture and Technology
Koganei 184-8588, Japan
M. Nemoto
Faculty of Environmental, Life, Natural Science and Technology
Okayama University
Okayama 700–8530, Japan

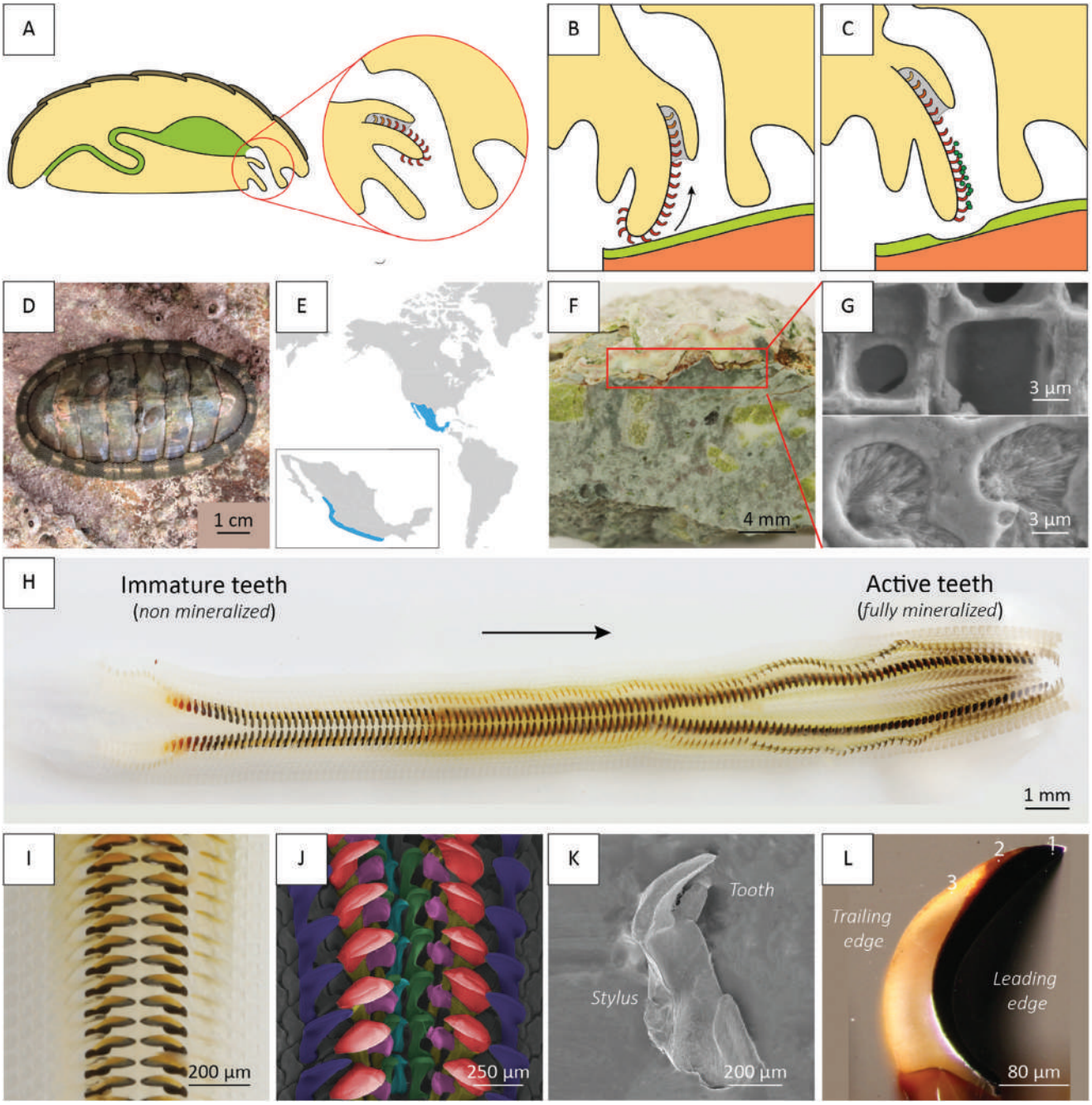

Figure 1. A) A schematic of a longitudinal section of the chiton showing the location and organization of the radula. B and C) show schematics of the motion of the radula during the feeding process. D) A photo of a Chiton articulatus, a mollusk endemic to the E) tropic Pacific coast of Mexico. F) is a photo of a typical rock the mollusk grazes on with a layer of crustose algae (red square) and an example of those mineralized coralline algae G). H) An optical micrograph of an entire radular belt with an arrow identifying the direction of the maturing teeth and I) a higher magnification micrograph, providing insight into the arrangement of mature teeth. A false-colored scanning electron microscope (SEM) micrograph of the radula is reported in J), with the teeth highlighted in red, while an extracted mature tooth and its stylus are shown in K). L) an optical micrograph of a longitudinal section of a mature tooth with numbers identifying the three main regions of the tooth.

observed distributed in the whole tooth section. N, S, and Cl were primarily located in Regions 1 and 2 while Mg, Na, and Si were predominantly located in Region 3. No preferential location was attributed to K. The EDS analyses showed no large compositional gradients at the interfaces between Regions 1, 2, and 3. However, this analysis highlighted the presence of an additional region represented by the interface between the tooth and the supporting stylus, the junction zone.[64,65] This region had significant concentrations of Fe, Ca, P, Mg, and O. Despite that, this region was not as heavily mineralized as the tooth so it was

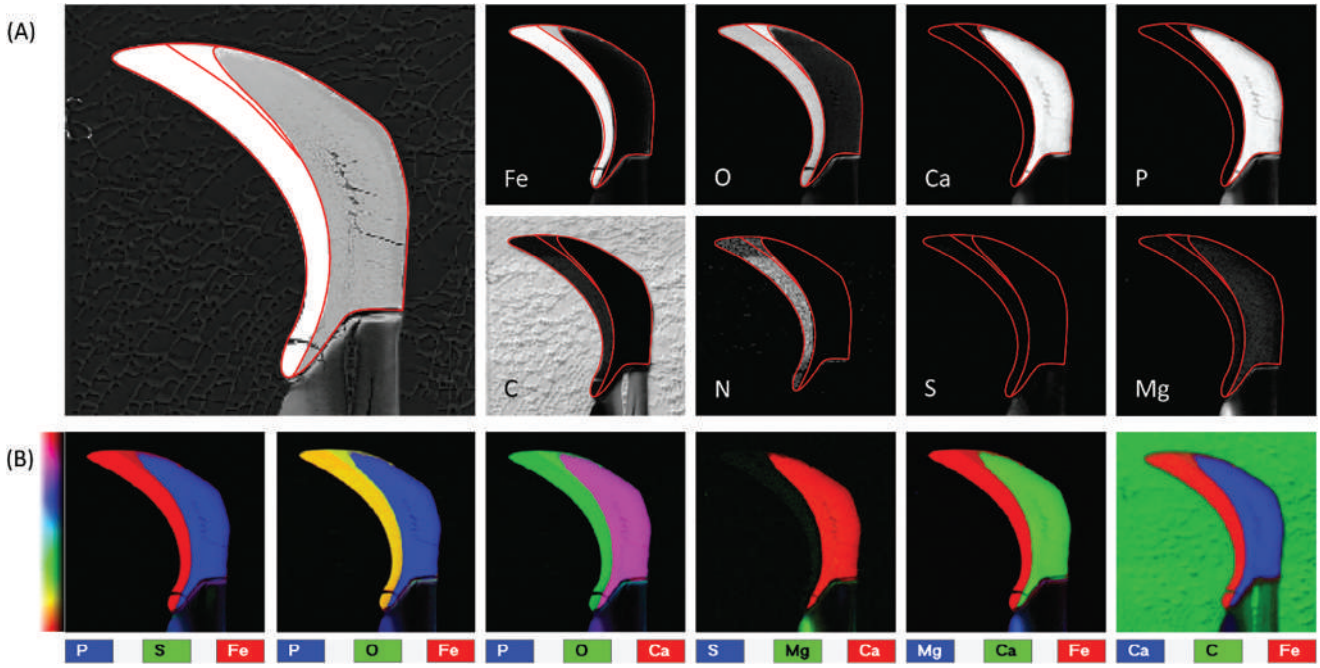

Figure 2. A) EDS/XRM-SEM analysis of a mature tooth longitudinal section revealed the distribution of different elements. A red line profile defines the three different regions in the tooth. B) Pseudo-colored X-ray maps highlight the correlation between the main elements present. Primary colors (red, green, blue) denote the main elements whereas secondary colors (yellow, magenta, cyan) denote a correlation between the two.

considered part of the stylus and will be discussed in a future work.

Correlation maps between different elements showed two different Fe/O correlations in Regions 1 and 2, and a correlation between Ca, P, and O in Region 3 (Figure S2 and Table S1, Supporting Information). No correlation was found between Fe and Ca, or Fe and P. In addition, in Regions 1 and 2, no correlation was found between P and O. Images and graphs related to the correlation between these elements are reported in Figure 2 and **Figure 3**. Correlation maps between Mg and other elements (Figure S3, Supporting Information) showed a slight correlation with Fe, as well as O in Regions 1 and 2. A visible correlation was observed with Ca, P, and O in Region 3. Since Regions 1 and 2 also showed a significant signal for elements usually associated with an organic matrix, a correlation map analysis for these elements was also performed.

X-ray diffraction of the whole tooth using a synchrotron light source showed the presence of multiple crystalline phases (Figure 3A): hydroxyapatite, magnetite, goethite, lepidocrocite, as well as one organic-based semicrystalline phase, α-chitin. The distribution of these mineral phases was studied by using a line scan function via Raman microscopy (Figure 3B,C). The data showed the presence of α-chitin in all regions and that the magnetite phase is located in Region 1, while Region 2 consists of a mixture of lepidocrocite and goethite, and Region 3 is comprised of hydroxyapatite. Additional point scans were conducted and found no discernable difference in the local concentrations of lepidocrocite and goethite in Region 2, with the intensity of the peaks for both phases showing no regional variation.

2.2. Architecture and Self-Sharpening

A SEM study was conducted on both polished tooth sections treated with NaClO to highlight the mineral organization in both polished and broken tooth specimens. Different microstructural morphologies were found associated with each of the different regions (**Figure 4**). On the very leading edge of the tooth (periphery of Region 1), a nanoparticle-based morphology was observed (Figure 4C). The nanoparticle area of Region 1 then appears to transition to a more orientated and lamellar microstructure, with its long axis initially aligned parallel to the leading edge, closer to the nanoparticles, but reorienting perpendicular to the leading edge about halfway through the thickness of Region 1 (Figure 4B). This change in morphology was observed within the area highlighted in Figure 4B, where nanoparticles appear to preferentially aggregate into clearly visible lamellae (Figure 4D). This lamellar organization was observed only in the top half of the tooth, immediately adjacent to Region 2. The microstructure of Region 1 in the lower half of the tooth showed only nanoparticles with no significant alignment. For Regions 2 and 3 (specifically near the top quarter of the tooth), continuous lamellae were observed transversing both regions (Figure 3E), with a change in microstructure associated with each of these regions. Region 2 shows a lamellar texture of plate-like nanosheets but is less preferentially oriented compared to the structures observed in Region 1 (Figure 3F). Region 3 consists of what appear to be oriented structures, with a much finer texture prohibiting the identification of single features in SEM. A similar curvature and orientation of nanoparticles and lamellae were also observed on transversally broken sections at the leading and trailing edges of the tooth (Figure S4, Supporting Information).

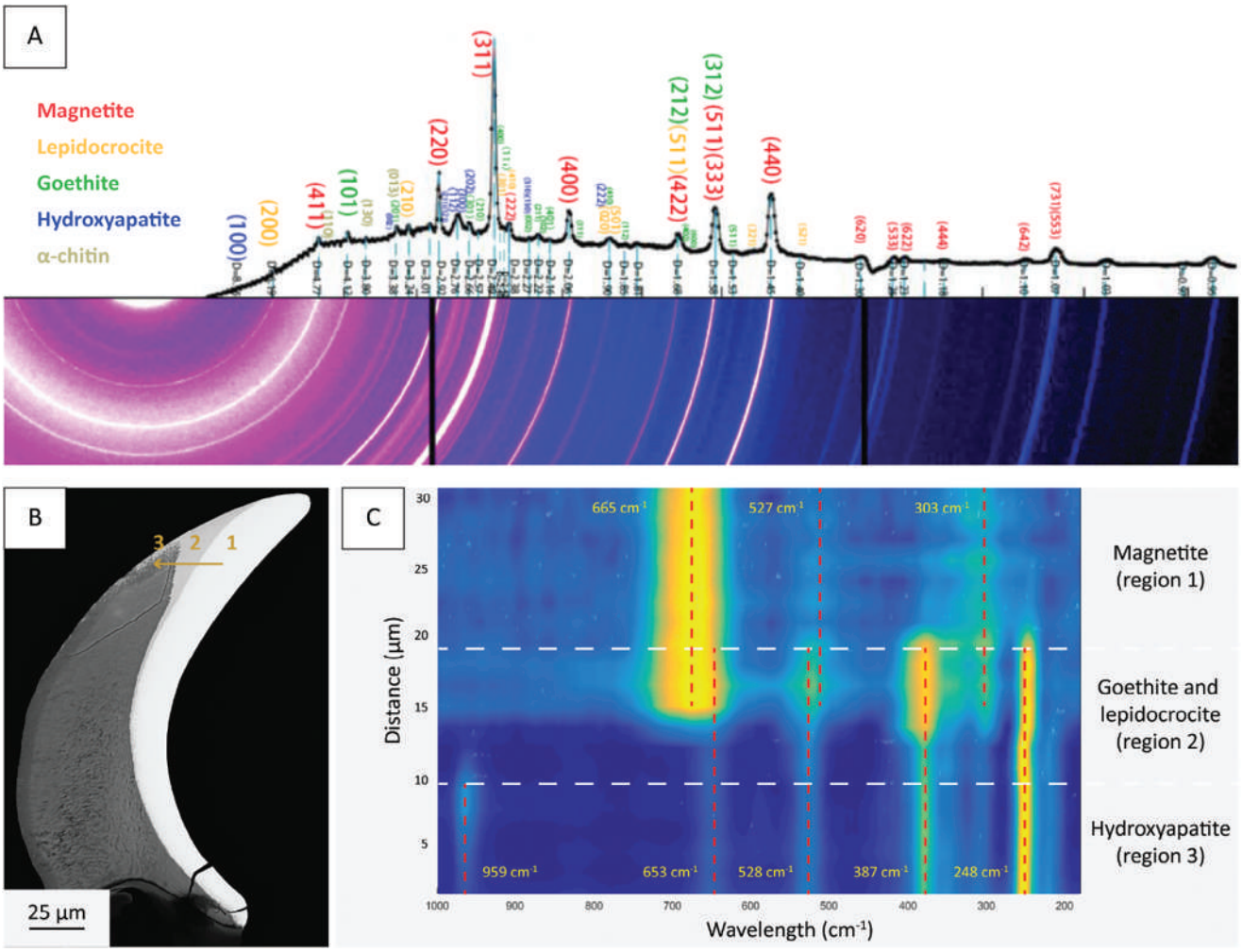

Figure 3. A) Synchrotron X-ray diffraction analysis of a mature tooth taken from 3 diffraction frames. Peaks indexed and colored to correspond with identified crystalline phase listed on the left. Backscattered Electron micrograph B) of a longitudinal tooth section with an arrow showing the direction and relative location of a C) line scan analysis done using Raman spectroscopy. The resulting heatmap denotes the intensity of peaks and subsequent characterization of the phases present shown to the right.

Upon fracturing teeth, a strong preference for the cleavage surface was observed. Most of the samples broke following the orientation of the nanoparticles and lamellae. This was observed to form a convex surface of cleavage in the tooth with the maximum located at the nanoparticle-lamellae interface within Region 1. This behavior was also observed in longitudinal sections with respect to the leading edge of the tooth, allowing us to observe areas that transitioned between morphologies.

Complete demineralization of a transverse section from an embedded and polished tooth was performed using oxalic acid 0.3 M (see Figure S5, Supporting Information). In this sample, it was possible to observe layers of fibrous organic matrix that compartmentalize the different regions of the tooth. A structurally intact organized organic matrix in Region 1 was observed. This matrix was a highly aligned porous matrix following the orientation of the mineral observed. It was not possible to observe the same result on a longitudinal section due to the complete loss of the organic matrix.

Using a Focused Ion Beam (FIB), sections of the interfaces between Region 1 and 2, as well as Regions 2 and 3 were prepared, and imaged in Transmission Electron Microscopy (TEM) (**Figure 5**). Micrographs of the intersection between Regions 1 and 2 reveal a unique arrangement of the two phases, with evidence of rod-like structures of goethite and magnetite intertwining with each other. EDS in (Figure S6B, Supporting Information) of this region shows little to no difference in the distribution of the constituent elements present, specifically iron and oxygen. However, Selected Area Electron Diffraction (SAED) confirms the local presence of both phases in these rod-like arrangements. Between Regions 2 and 3, a suture-like area was observed exhibiting a well-defined arrangement, serving as an interlocking junction between the lepidocrocite and hydroxyapatite regions. The micrographs reveal an intricate nanostructure, with hydroxyapatite crystallites and larger lepidocrocite needles supported by an organic matrix (Figure S7, Supporting Information). Moreover, elemental mapping and spectroscopic analysis using EDS in TEM (Figure S6C, Supporting Information) elucidated the

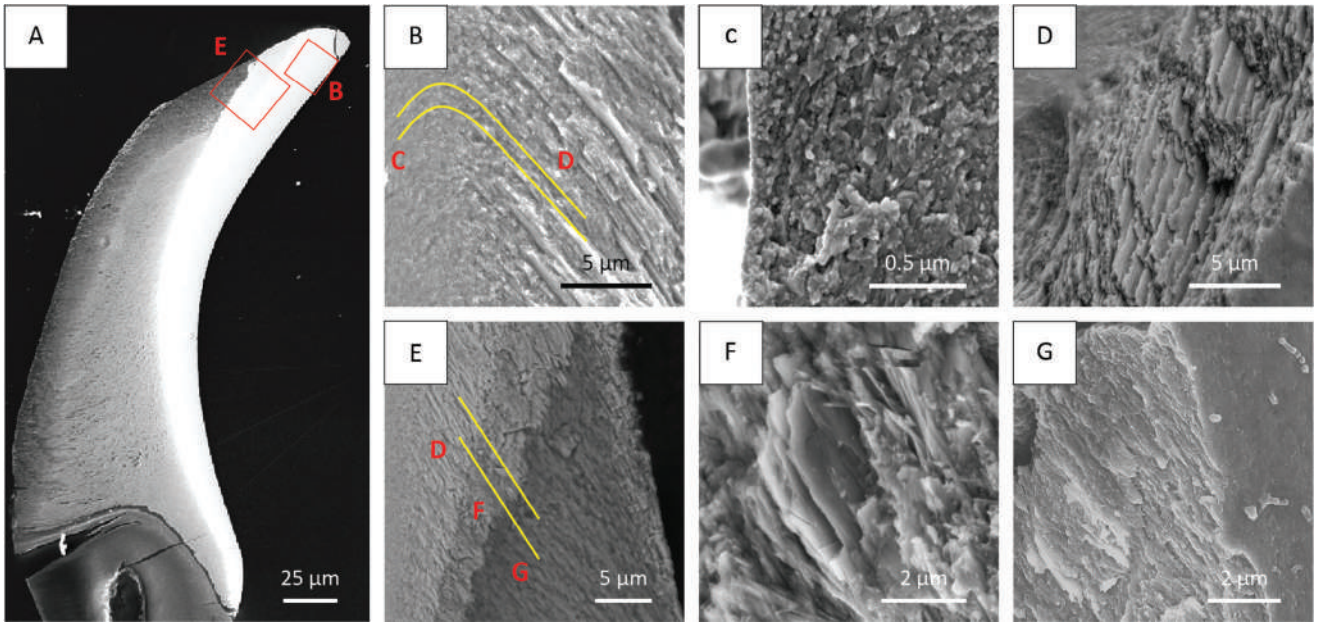

Figure 4. A) Backscattered SEM micrographs of a longitudinal section of a mature tooth. B) Conversion between C) nanoparticles and D) lamellae in Region 1 (magnetite), yellow lines highlight microstructural orientation. E) Backscattered SEM micrograph of the different regions in the sample showing a continuous lamellar organization (yellow lines). SEM micrographs of the lamellae in F) Region 2 and G) Region 3.

elemental distribution and composition of this suture-like interface. The results indicate a distinct transition from a predominantly iron oxide-rich composition to a calcium phosphate-rich composition, suggesting a non-gradual change in the mineralization process during tooth formation. Further observation of the nucleation and growth of these phases within the biogenic system is being studied to provide insight into the development of these rod and lamellar structures in addition to these suture-like interfaces.

Nanoindentation analysis was performed on a tooth longitudinal section to elucidate the mechanical properties of each region. The analyses showed the presence of four distinct areas with different hardness (H) and reduced Young's modulus (RYM) values (**Figure 6**). Two of these areas, where nanoparticles and lamellae are present, were associated with Region 1, while the remaining two areas corresponded to Regions 2 and 3. The corresponding H and RYM associated with these areas decrease when moving from the leading to the trailing edge.

In this species, worn teeth can be observed in the active region of the radula. These teeth were singularly extracted and observed using SEM (**Figure 7**). As expected, the micrographs reveal that wear increases with the maturity of the teeth (where "n" would be the most mature tooth on the radula). The height of each single tooth was measured to quantify the amount of wear on the tooth. A gradual decrease in height was observed from tooth n-16 (no

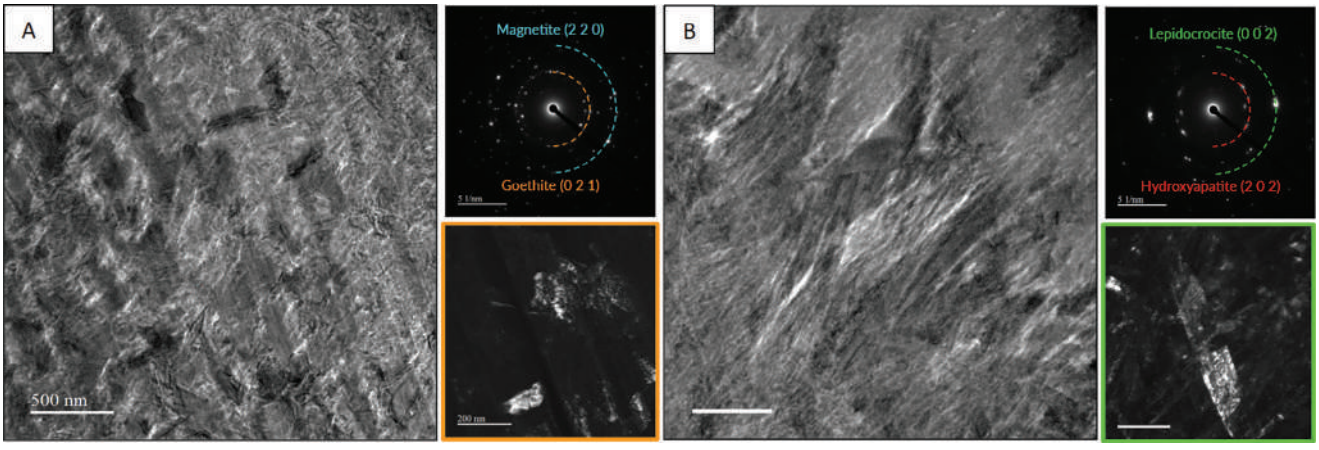

Figure 5. TEM micrographs showing the transitions between A) Region 1 and 2, and B) Region 2 and 3. SAED patterns show the presence of each of the iron oxide and calcium phosphate phases. Spots equidistant from the center of the diffraction pattern result in the overlayed ring which corresponds to diffracted planes of the polycrystalline phase present.

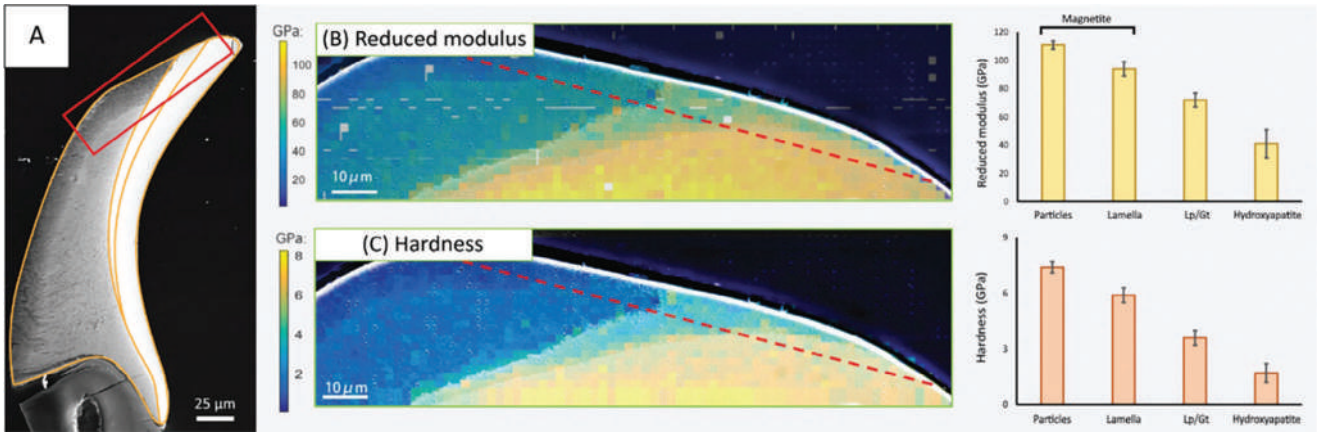

Figure 6. Nanomechanical properties of a mature tooth. A) Back scattered SEM micrograph of a longitudinal section of a mature tooth, orange lines identify the different phase regions while a red box indicates where nanoindentation was conducted. B) Reduced modulus and C) hardness maps in the sample, with a correlating histogram reporting the numerical values in the different regions of the tooth.

observable wear) up to about half of the initial height of an intact tooth (i.e., by tooth n-6). No additional decreases in height were observed in the last 6 teeth of the radula. Along with the height, the angle at the tip of the tooth was also measured. A gradual increase in the angle was observed between tooth n-16 to n-4, from ≈30° to 80°. From tooth n-4, a significant increase in this angle was observed in the last 3 teeth (i.e., to tooth n-1), returning to ≈50°. Tomographic analyses of the tooth revealed that a change in the ratio of surface areas for each of the three regions at differing levels of wear is present, exposing more of the hydroxyapatite region as the tooth is worn down. At approximately half of the height of the tooth, Region 2 was no longer observed. Nanoindentation maps of the corresponding planes showed that these different exposed surfaces (i.e., phases) are associated with different mechanical resistances.

2.3. Modeling of Crack Propagation

In its feeding process, *C. articulatus* employs its radula to perform a rasping motion across the substrate, utilizing scraping and grinding actions of the teeth to extract food particles from rocky substrates. These teeth encounter varying resistance and hardness in the feeding substrate, and the organism needs to dynamically adjust its forces to feed effectively. Hence, from the modeling point of view, this intricate motion is considered to be predominantly load-controlled. Consequently, the stress concentration across the tooth exhibits only geometry-dependent characteristics from the perspective of bulk material modeling. A 3D Finite Element Analysis (FEA) was conducted on the *C. articulatus* tooth geometry that was obtained from micro-CT scans and was simulated under quasistatic conditions, utilizing a dynamic implicit solver in ABAQUS CAE. The base of the tooth was fixed, and displacement-controlled loading was applied at the tip of the tooth in the leading to trailing direction. The deformation was assumed to be finite and linear elastic. Examination of the normalized maximum principal stresses distribution across the tooth revealed tensile forces on the leading edge and compressive forces on the trailing edge as expected from theory of cantilever beams.

Furthermore, stress distribution contours of normalized maximum principal stresses were extracted across three distinct cross-sections: sagittal, coronal, and transversal as shown in **Figure** 8A. Upon examining stress contours in the 2D profiles of the three cross-sections, the 2D longitudinal profile proves dependable and as a simplified proxy for the 3D model. This reliability is supported by a consistent correlation observed between the 2D stress profile from the longitudinal view and the more intricate stress distribution in the comprehensive 3D model. Thus, simplifying the 3D model into a 2D representation using plane strain conditions across the longitudinal plane becomes a more feasible approach for the next steps of modeling that involves analysis of crack propagation. Specifically, our focus is on understanding how the inherent material gradient influences the trajectory of crack propagation across the tooth under varying loading conditions and initial crack locations. The overarching objective is to assess whether these factors contribute to self-sharpening mechanisms, especially since previous literature has underscored the significance of material gradients and their influence on crack propagation.[66] Experimental studies on crack propagation in the teeth are challenging due to limitations in controlling variables. However, FEA models offer a solution for a more thorough analysis by simulating the actual tooth gradient and comparing results across various user-defined scenarios.

We conducted an initial investigation focused on the propagation of cracks across a 2D profile of the articulatus tooth. Figure S8 (Supporting Information) demonstrates the variation in crack propagation paths across a standard tensile test of a single-edge cracked rectangular plate undergoing mode-1 fracture in response to changing layered material gradients. Additional information on the influence of factors such as stiffness and peak load are also provided in supplementary materials.

In this study, the extended Finite Element Method (XFEM) was employed to analyze crack propagation across the 2D longitudinal profile of the *C. articulatus* tooth, considering four cases of layered material distribution: a heterogeneous model (HM) representing what is observed in nature, and as measured experimentally via nanoindentation, a reverse heterogeneous model (RHM), a homogeneous-all-magnetite model (HAMM), and a

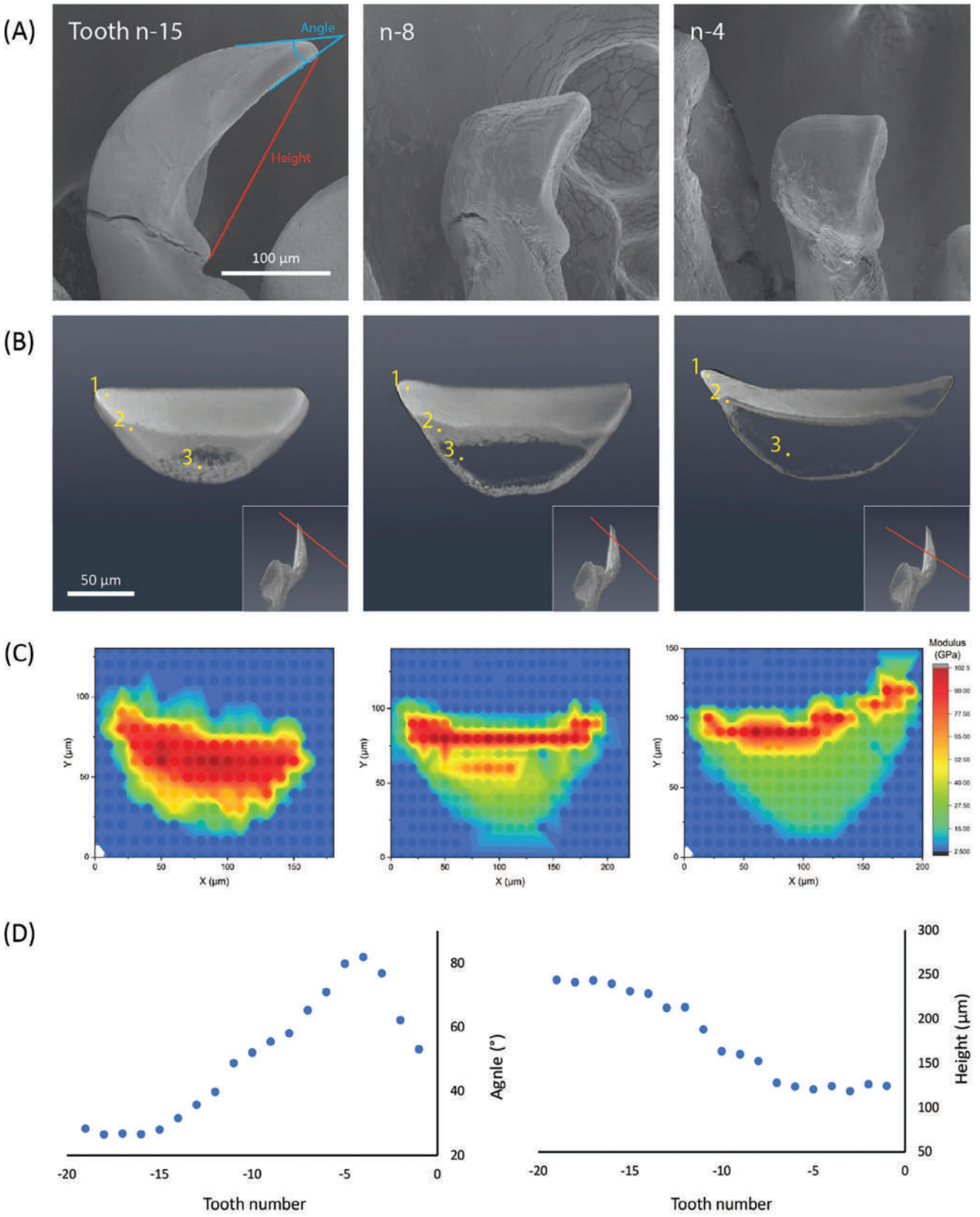

Figure 7. Self-sharpening effect of the teeth in C. articulatus. A) SEM micrographs of teeth in different positions along the radula belt's active region; yellow and red segments indicate how height and angle were measured on the worn teeth. B) Tomographic scan planes and C) nanoindentation maps corresponding to the exposed surfaces of the worn teeth reported in A. D) Angle and height of the mature teeth in the active region of the radula.

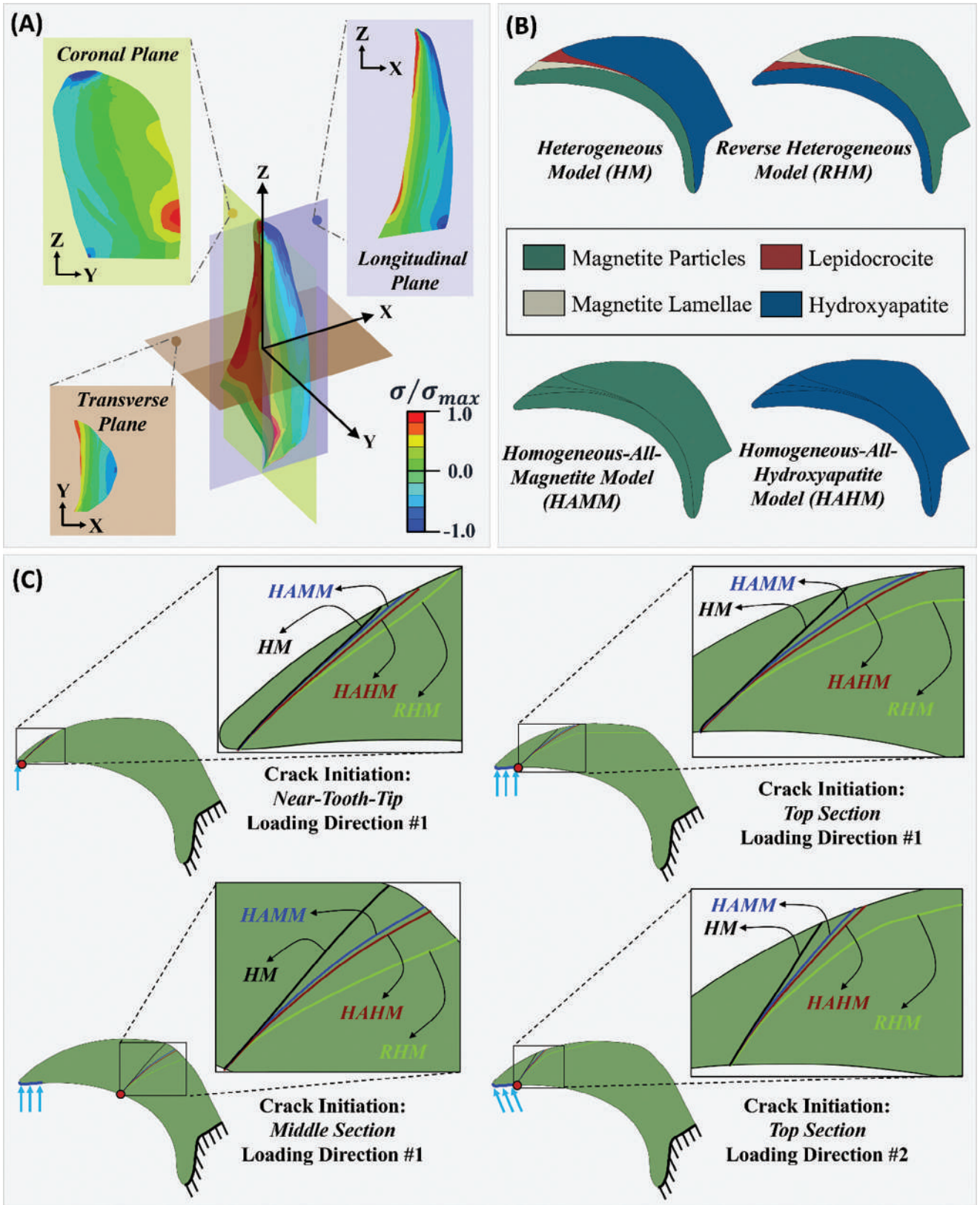

Figure 8. Computational Modeling of the articulatus tooth. A) 3D FEA analysis of the articulatus tooth showing the contours of normalized maximum principal stresses across the tooth, along with three cross-sectional views in the coronal, sagittal and transverse planes. B) Enhanced 2D longitudinal geometry profile as taken from SEM images with four cases of material gradient distributions across the surface — HM, RHM, HAMM, HAHM. C) XFEM models showing crack propagation trajectories across the surface of the tooth for all the four material gradient cases when subjected to four types of boundary conditions as described.

homogeneous-all-hydroxyapatite model (HAHM) as shown in Figure 8B. XFEM was used here to simulate the crack propagation as it allows for initiation and propagation of a discrete crack along an arbitrary, mesh-independent path,[67] enabling a more realistic capture of crack trajectory in natural systems like the *C. articulatus* tooth. The tooth was simulated under plain strain assumptions under quasistatic loading using a dynamic implicit solver. Boundary conditions were carefully selected to closely emulate real-life constraints while being mindful of 2D modeling assumptions. To replicate the natural connection between the tooth and stylus, the bottom edge section of the tooth was fixed, highlighted in black in Figure 8C. The study included the initiation of cracks at three distinct locations along the tooth: near the tooth tip, the top section, and the middle section, as illustrated in Figure 8C and marked with a red dot. The first case involved displacement-controlled loading at the tip, while for the remaining cases, the load was applied at the top section edge of the tooth, visually emphasized in dark blue. In the top section case, where the impact of material gradient is most notable, additional simulations were conducted to examine the effect of loading direction, represented by arrows in light blue. In total, 12 XFEM simulations were performed for this study, and the propagated cracks were presented as an overlaid image with a zoomed-in inset highlighting the crack paths. This methodology allowed for a comprehensive preliminary analysis of variations in crack trajectory based on material gradient distributions, initial crack locations, and loading directions.

3. Discussion

In this study, the composition and architecture, as well as the resulting mechanical properties of the mature teeth of *Chiton articulatus* were examined. Among the teeth present in the radula, we chose to focus on the mature ones present in the distal region of the radula since these would be the ones utilized in the feeding process. In fact, during the feeding process, these teeth, which are connected to a stiff yet flexible stylus,[65,68] make direct contact with the hard rocky substrates upon which the animal grazes to collect organic materials such as hard coralline algae. These interactions result in contact stresses and thus, the material composition and architecture of the tooth must be sufficiently hard and tough.

Optical (Figure 1H) and SEM (Figure 2A) micrographs provide observations of a longitudinal section of this monocuspid mature tooth and revealed the presence of three distinct regions. EDS (Figure 2) shows that both Regions 1 and 2 both consisted of iron-rich minerals, whereas Region 3 contained calcium and phosphorus-based mineral. Subsequent the use of X-ray diffraction analysis using synchrotron light combined with Raman spectroscopy confirmed that Region 1 was dominated by magnetite (Fe_3O_4), which is an ultrahard phase also observed in other species of chiton.[31,32,34,69,70] Thus, the presence of this hard phase is not surprising, as we surmise that this organism is rasping on rocky substrates that are encrusted with coralline algae, which necessitates the presence of a harder mineral on the leading edge of the teeth.[70,71] The same analyses also showed that Region 2 of the tooth consists of other iron oxide phases, lepidocrocite (γ-FeO(OH)) and goethite (α-FeO(OH)), while Region 3 (observed close to the trailing edge and extending to the bulk of the tooth volume) was found to consist of the hydroxyapatite ($Ca_{1n}(PO_4)_6(OH)_2$) phase.

3.1. Presence of Minor Elements

It was interesting to observe how minor elements are distributed in the different regions of the tooth. Na, Mg, and Si tend to concentrate in Region 3 with Na having a concentration up to 8 times higher if compared to its concentration in Region 1. This accumulation may suggest that, as it occurs in other biomineralizing marine organisms,[72] the Ca ions necessary for hydroxyapatite deposition may be concentrated directly from seawater. This would induce an accumulation of secondary minor elements, such as the ones found, that were not entirely removed by the organism. Na and Mg ions are also theorized to be involved, combined with chitin-binding proteins, in the mediation of the interaction between minerals and crystalline chitin fibrils.[73]

Additionally, the correlation observed between Mg and Ca, P, and O is not unexpected. This element has crucial importance in biomineralization, especially in that of Ca-based biominerals. In calcium carbonate, for example, a minor amount of Mg strengthens the crystal making it harder.[71] In hydroxyapatite, on the other hand, the presence of a minor amount of Mg has been observed to decrease the crystal size due to a clustering of the crystal lattice around Mg-substituted Ca-sites.[74,75] This last effect would explain the lower crystallinity observed in Region 3. A correlation between Mg and Fe was also observed in Regions 1 and 2, suggesting the presence of a magnesium-enriched phase. On the other hand, the possibility of having Mg and Na mediating between chitin fibrils and mineral is likely to be possible considering their lower concentration.

Chlorine was another element with an interesting distribution since, despite the main presence of cations in Region 3, Cl was found to be concentrated primarily in Regions 1 and 2. This higher Cl presence may be counterbalanced by the higher amount of organic phase in these regions, thus working as a counter ion. In fact, a significantly higher signal for N, and S was observed. Correlations between Fe and C were observed as a hint that a higher amount of organic phase was present with specific interactions with the mineral phase. These observations find confirmation in the demineralized matrix, where a stable framework of the fibrous organic matrix was observed. This matrix likely contains a significant amount of crystalline α-chitin observed using X-ray diffraction. The higher amount of S observed may be associated with protein sulfonation, a post-translational modification previously observed in proteins involved in biomineralization. Another possibility may be the presence of disulfide bridges, frequently observed in chitin-binding domains.[76] Considering the diffusion in the correlation between C and S from the EDS maps, both scenarios are likely to be possible. The ionization of the protein matrix and the increased number of chitin-binding sites would combine with the mediation between mineral and chitin-binding proteins due to Na and Mg. These features would surely induce a positive influence in reinforcing the matrix, by increasing the interaction of proteins with the mineral phase and the chitinous scaffold.

3.2. Microstructural Transformations

Furthermore, evaluation of the microstructural features within Region 1 demonstrated multiple morphological features: nanoparticles and rod-like lamellae. The nanoparticles, located on the outermost periphery of the leading edge, transition into a lamellar morphology with a distinct change in orientation (Figure 4B–D). This second morphology was only observed in the top half of the tooth. The observation of nanoparticles at the very surface of the tooth is something that has been observed before, in the mineralized teeth of *Cryptochiton stelleri*.[70,77] The nanoparticles are the morphology in direct contact with the substrate during the feeding process. Nanoparticles offer a strong advantage in dissipating energy compared to lamellae since they can dissipate part of it by rotation or displacement other than cracking. Moreover, compared to lamellae any crack forming in the material would find, regardless of its directionality, more interfaces while propagating due to the isotropic alternation of organic layers and mineral particles. These advantages may be the reason behind the evolution of this morphology which would help dissipate the stress accumulated during feeding or rasping events. A well-studied example of this effect is the dactyl club of the mantis shrimp, where a protective nanoparticle coating is present.[78] The presence of a mild nanoparticle alignment also suggests an additional adaptation. In correspondence with the aligned particles, a layer with fewer organic-mineral interfaces is present. The lack of interfaces would allow a crack to propagate in that direction while continuing to branch laterally. This would allow the matrix to propagate cracks in the direction of the tooth tip rather than the bottom. Although we surmise that these particulate coatings function as a protective layer against locally high contact stresses, we will address it in future work.

After these initial nanoparticle layers, the mineral phase interconverts gradually into a lamellar morphology. Associated with this change in morphology a change in the alignment orientation is observed, now almost parallel to the trailing edge surface. The rod-like elements have also been observed as well and have been shown to provide strength under tension or compression during rasping events.[32,70] While the nanoparticle-based surface of the leading edge of the tooth may mitigate local contact stresses, the combination of anistropic rods within lamellae and the different material phases (i.e., magnetite, goethite, lepidocrocite and hydroxyapatite) are likely responsible for the self-sharpening features observed in these teeth (Figure S9, Supporting Information).

3.3. Self-Sharpening Capabilities

A similar use of lamellar structures to achieve self-sharpening has been observed in other species, such as sea urchins[71] or other chiton species.[30] In *C. articulatus*, this effect is attributed to and further amplified by the utilization of different materials and phases, leading to a gradient in hardness and modulus (decrease in H and RYM moving from the leading edge to the trailing edge). Specifically, damage caused by abrasion can occur by localized plastic deformation against a blunt and rigid contact (e.g., the rocky substrates upon which the teeth rasp). In this case, the critical normal load for yielding P_y (according to Hertzian contact mechanics) is proportional to the materials property group, $P_y \infty H^3/E^2$, where hardness is dominant.[31] With the significant difference in hardness between Regions 1, 2 and 3, preferential wear will occur on the softer phase materials, leading to the self-sharpening phenomenon. The final effect of these adaptations can be observed in the results summarized in Figure 6. Figure S10 (Supporting Information) depicts the overall wearability of these teeth in relation to average regional values for P_y showing that the hydroxyapatite region would wear preferentially as P_y decreases. Despite the teeth losing up to half of their height, a gradual decrease in the tooth angle is observed as proof of the teeth counterbalancing the substrate abrasion.

Observing the height of the tooth in the active region, it can be seen that each tooth stops wearing off at about half of its height (e.g., tooth n-6). The tooth angle is also observed to stop increasing at that point. These two results suggest the tooth is likely too short to properly interact with the substrate. At the same height (i.e., half the height of the tooth), Region 2 is no longer present and the lamellae in Region 1 are reduced, leaving only a large fraction of the softer Region 3 and the nanoparticles in Region 1. Past tooth n-6, an increase in the tooth angle is observed in the last teeth of the radula after this point. This change may suggest that, despite not being able to interact with the substrate properly (or with enough energy applied), the tooth may contact higher topological points on the rock, preferentially interacting with the softer posterior region of the tooth.

It should also be noted that there is no delamination or failure present within phases or at their interfaces within the teeth. The presence of an organic phase, which has been documented in other chitons,[70] provides a significant toughening effect to dissipate energy via crack deflection. There is a decrease in the relative thickness of lamellae moving from the leading to trailing edge in Regions 1 and 2, suggesting a change in the rod element thickness within these lamellae and therefore an increase in the number of mineral-organic interfaces. These interfaces of dissimilar elastic moduli are known to provide significant toughening.[79] Beyond the materials used, their arrangement also provides toughening at interfaces. The suture organization between the iron oxide and calcium phosphate regions is thought to contribute to the overall toughness of the teeth by preventing catastrophic failure and delamination between the regions when subjected to abrasive forces, much like the microstructure within our own teeth,[80] ensuring structural integrity and overall long-term functionality.

Evolutionarily speaking, the tooth from *C. articulatus* shows major similarities with that described for chitons in the *Acanthopleura* and *Chiton* genus in terms of composition and general organization.[29,81,82] In these chitons, a magnetite region on the leading edge, followed by an iron hydroxide intermediate section, and a trailing edge of apatite is observed to have similar macroscopic organization. Despite that, the only paper mildly documenting the microstructure of the tooth is from *A. echinate*, where an orientation of the texture analogous to that observed in *C. articulatus* is described.[82] However, the study does not examine the morphology in depth. While there is no reference to nanoparticles due to the emphasis on the elongated morphologies observed, these structures may still be present. A more in-depth analysis of the microstructure was performed on

Acanthochiton rubrolineatus.[30] In this species, an aligned rod organization was observed following the same alignment in *C. articulatus*, no nanoparticles were observed in this species. Despite that, this species presents a magnetite shell and an iron phosphate core organization similar to that of *C. stelleri*. It is interesting to observe how the teeth of A. *rubrolineatus* are described to be visibly worn off in the active zone. *C. stelleri*, on the other hand, showed a magnetite shell composed of nanorods running parallel to the surface.[31] Contrary to the previous species mentioned, no significant wear is observed in the teeth of this chiton. This difference may arise from the different feeding habits of *C. stelleri*, mostly consuming softer algae. Thus, the combination of architecture and material components of *C. articulatus*, which has a more robust interaction with the rocky substrates, have been tuned to provide effective feeding on these hard substrates, while mitigating catastrophic fracture.

Combining the observations of the organic framework in the demineralized sample with the mineral texture and morphology, we suggest that thin organic layers are present in between nanoparticles and lamellae. The presence of organic layers between mineral elements is a common feature in biominerals, already observed in shells[14,20,83] as much as in other chiton teeth.[31] In fact, many of these biological composite materials provide a pre-assembled structural organic (e.g., chitin) that, coupled with proteins guides the final architectural features.[84] Of course, the additional advantage of having this organic phase present between mineral domains is that the mechanical properties of the material, specifically toughness, are improved by controlling crack propagation at interfaces.[19,70,85]

3.4. 2D Finite Element Analysis

The findings from the computational models indicate a discernible impact of material gradients on crack propagation and, hence on tooth wear, which leads to the self-sharpening effect. Across various loading scenarios and initial crack locations, HM consistently exhibited the least amount of tooth wear. In the case where the crack initiates at the tip, the difference in crack paths is minimal, as the material gradient plays a minor role at the tip surface. However, in the top section, where the material gradient has a more substantial impact, notable differences in crack paths are observed, with the HM model consistently showing the least tooth wear for both loading directions. Despite RHM performing poorly, although it represents an idealized opposite case compared to the real scenario, it serves as a model highlighting the importance of the correct order of distribution of material gradient for selective self-sharpening. Both homogeneous cases, HAMM and HAHM, perform similarly, exhibiting more tooth wear than HM but less than RHM. Shifting the initial crack to the middle section of the tooth reveals differences in crack trajectories, albeit less pronounced than when the crack initiates at the top section, as the significant role of the layered material gradient starts to diminish beyond this region. This observation aligns with the existence of a wear height threshold for the articulatus tooth, beyond which self-sharpening becomes unnecessary, given the disuse of the tooth during feeding. Furthermore, HM demonstrates a more linear trajectory for crack propagation, suggesting a mechanical advantage that contributes to enhanced structural resilience, improved load distribution, and controlled energy release during crack propagation. These findings underscore the substantial role of the material gradient in crack propagation, contributing to the self-sharpening effect. They imply that the tooth exhibits a preferred material gradient distribution, striking a balance that fosters self-sharpening while maintaining optimal stiffness for sustained cutting strength during feeding.

Nevertheless, our study recognizes the need to further refine the modeling approach to develop a continuous progressive crack propagation model using XFEM. This involves sequentially initiating the first crack at the top, allowing it to propagate, and extracting the geometry of the failed tooth. The obtained geometry will then be subjected to similar conditions, and the process iterates until the minimum height is achieved, as observed in SEM analysis images. This comprehensive analysis will be extended to all four material distribution gradient models and various loading directions in future work. In the present work, only two loading directions and three initial crack locations were used and were all selected arbitrarily from observations made during its rasping behavior while feeding. Additionally, future investigations will address the influence of microstructure orientation within the tooth, followed by an exploration of the combined effects of microstructure and material gradient distribution in both 2D and 3D models.

4. Conclusions

In this study, the composition, microstructure, and mechanics of the teeth of *C. articulatus* were investigated. Like other species previously examined in the literature, this species shows visible wearing of the teeth in the active region of the radula. This is likely due to its diet, including hard coralline algae strongly connected to the rocky substrate upon which the animal feeds.

A hard organic-rich nanoparticle-based magnetite layer covers the leading edge of the tooth and during feeding is in direct contact with the substrate. Behind that, a succession of different lamellae with decreasing hardness' and stiffness' as well as finer textures were observed transitioning through different compositions (magnetite, lepidocrocite/goethite, and hydroxyapatite). This graded architecture leads to a self-sharpening structure as suggested from 2D Finite Element analyses. Interesting features have also been observed in the organic matrix present in the Fe-rich regions of the tooth. The presence of minor elements is likely involved in increasing the interaction between the mineral phase and the chitinous scaffold that guides regional architectures of the tooth. This connection would represent an additional strengthening present in the matrix. Furthermore, the presence of organic material at the mineral interfaces can toughen structures within the tooth via crack deflection.

Prior to this study, there has been no comprehensive material-based examination of teeth belonging to the Chiton genus. Moreover, no study has addressed the self-sharpening of a chiton tooth while considering both morphological and compositional features. The novel information collected in this study will help to understand the mechanics of this and other analogous biogenic systems, leading to important innovations in abrasion-resistant and self-sharpening materials. This knowledge will also strongly contribute to the understanding of the evolution and feeding

habits of this and other chiton species, shedding light on their biodiversification.

5. Experimental Section

Specimen Collection: Adult specimens of *Chiton articulatus* (n = 70; 40 mm ≤ total length ≤ 80 mm) were collected from the rocky intertidal shore of Barras de Piaxtla, Sinaloa, Mexico (23°38′51.0″ N 106°48′16.6″W) at the northern limits of its geographical distribution, following collecting regulations established under Mexican law (NOM-126-SEMARNAT-2000). Specimens were relaxed by leaving them in a refrigerator at 7 °C for 30 min before dissection, following regulations for the humanitarian sacrificing of animals as established under Mexican law (NOM-033-SAG/ZOO-2014). Subsequently, the radulae were removed from the oral cavity of each chiton, stored in water at 4 °C individually in Eppendorf tubes and away from further exposure to heat and light until the subsequent processes.

Optical Microscopy: The samples for optical microscopy were either directly laid on a glass slide and observed, or embedded in epoxy resin (US Composites), cut with a diamond saw, and polished using either silicon carbide films (3 M) or with a series of polycrystalline diamond suspensions (Allied). In both cases, optical micrographs were acquired using a Zeiss A2m equipped with a Canon 60D camera for transmission images or using an AmScope microscope equipped with an MU500 camera.

Raman Spectroscopy: Raman Spectroscopy scans were acquired from a polished sample, which was embedded in an epoxy resin and prepared as described above. The Raman line scan was recorded using a Horiba LabRam/AIST-NT with a research-grade Leica DMLM microscope (532 nm laser at 60 mW) that was rastered from the leading to trailing edge with a 1-micron step size.

X-ray Synchrotron: Wide angle X-ray scattering (WAXS) was obtained at Soft Matter Interfaces (12-ID) at the National Synchrotron Light Source II (NSLS-II), Brookhaven National Laboratory, using a 3 GeV electron storage ring. Samples were cleaned with standard procedure (lightly bleached, washed, critical point dried) and mounted on a Kapton tape surface. A 2.1(V) x 25(H) µm beam was positioned vertical to the leading edge of the tooth and was focused on the intersection between the apatite and magnetite regions. WAXS data was collected using Pilatus 300k-W detector and stitched from 7 frames. The sample to detector distance 0.27392 m and the energy was indicated as 20 keV as an argument.

Scanning Electron Microscopy: The samples for Scanning Electron Microscopy (SEM) were either air-dried and broken using a scalpel, or embedded in epoxy resin (US Composites), cut with a diamond saw and polished using a series of polycrystalline diamond suspensions (Allied) down to 5 µm. Microstructural features of the minerals within the sample were emphasized by partially removing organics present at mineral boundaries via the treatment of the sample surface with a 0.25 M NaOH and 3% NaClO solution mixture for 1 h. Additional microstructural details were provided by demineralizing the samples. Complete demineralization was achieved by treating with a 0.3 M oxalic acid solution for 2 h. All samples were then glued onto double-sided carbon tape that was placed on an aluminum stub and subsequently coated with 5 nm of Ir prior to analyses using an FEI Magellan 400 XHR SEM at 3–5 kV and 13–25 pA. The heights and angles of worn teeth were acquired from SEM micrographs of properly mounted, air-dried teeth, which were previously extracted from the radula using forceps. Subsequent image analysis was performed using ImageJ.

Energy Dispersive X-ray Analysis and X-ray Mapping (XRM): A JEOL 7001F field emission gun scanning electron microscope (FEGSEM) with a Amptek SDD C2 Si_3N_4 window operated by the Moran Scientific Microanalysis and X-ray mapping system were utilized for all X-ray mapping and post processing.[86–88] Full-spectrum XRM's were collected at 15 kV accelerating voltage, 1024×1024 resolution and 60 ms per point from polished samples which were embedded in epoxy resin and subsequently carbon coated.

Transmission Electron Microscopy: The samples used for Transmission Electron Microscopy (TEM) analysis were embedded in epoxy resin, cut using a diamond saw, and polished using a series of polycrystalline diamond suspensions (Allied) down to 0.2 µm to expose a longitudinal section of the teeth. Samples were then loaded into a TESCAN GAIA3 SEM, where sections (≈100–200 nm thick) were cut and extracted using a focused ion beam (FIB) and mounted onto an Omniprobe holder. TEM imaging and EDS were conducted using a JEOL 2800 TEM operated at 200 keV.

Nanoindentation: The nanoindentation maps were acquired using a Hysitron TI-950 TriboIndenter Nanoindenter using a Berkovich indenter tip. Before indenting, samples were embedded in epoxy resin (US Composites) and polished using a series of polycrystalline diamond suspensions (Allied) along longitudinal or transverse cross-sectional planes down to 0.2 µm. To acquire regional hardness and modulus maps, a trapezoidal loading profile using either 1.5 or 5 mN was applied (i.e., 5 s loading, 5 s hold, 5 s unloading), with each indent spaced 2–10 µm apart. The unloading curve of each indent was used to calculate hardness and modulus values following the Oliver-Pharr method.[89]

Computed Tomography: An intact tooth-stylus structure was scanned using X-ray micro-computed tomography (µ-CT) (Skyscan 1172, Bruker, USA). Serially dehydrated samples were mounted to a 1 mm diameter steel pin using Loctite super glue liquid professional (Henkel, USA) and mounted on a chuck. For the scan, a rotation step size of 0.1125° and an exposure time of 10 sec was used. The acceleration voltage was 80 kV and the isotropic voxel size was 1.4 µm. The images and 3D reconstructed models were developed using Amira software (Thermo Fisher Scientific, USA). After reconstruction, cross-sectional dimensions were determined by creating triangular mesh models and saved into a 3D file extension format of the virtual reality modeling language (known as VRL or VRLM).

Computational Modeling: A 3D finite element model of the *C. articulatus* tooth structure was constructed and analyzed in the commercial software Abaqus/CAE, 2021. The tooth was modeled as a mesh of 67739 quadratic tetrahedral elements of type C3D10 using 3D data from micro-computed tomography (CT) scans and regio-specific modulus data from nanoindentation maps. For the 2D modeling, the tooth profile was simulated under plain strain assumptions using a mesh of 16384 linear quadrilateral elements of type CPE4R, and the crack propagation was simulated using extended Finite Element Analysis (XFEM). All models were simulated in quasistatic conditions, under displacement-controlled loading using a dynamic implicit solver. The assumptions include infinitesimal deformations, linear elastic and isotropic material properties, and disregard for microstructure effects.

Supporting Information

Supporting Information is available from the Wiley Online Library or from the author.

Acknowledgements

This work was supported by the Air Force Office of Scientific Research, Natural Materials and Systems Program, through a Multi-University Research Initiative (MURI, FA9550-15-1-0009) and the Mechanics of Multifunctional Materials and Microsystems Program (FA9550-20-1-0292). The work is also supported by the Army Research Office, Biochemistry Program (W911NF-20-1-0201), and the Institute of Global Innovation Research (GIR) at TUAT. Specimen collection was done under research permits (PPF/DGOPA-130/15 and PPF/DGOPA-110/21) granted to O.H. Avila-Poveda by SAGARPA (currently Secretaria de Agricultura y Desarrollo Rural "SADER") through Comision Nacional de Acuacultura y Pesca "CONAPESCA". Welfare, humanitarian sacrifice and ethically responsible research with chitons were following the ethical recommendations for the humanitarian sacrifice of animals as established under Mexican law (NOM-033-SAG/ZOO-2014). O.H. Avila-Poveda was supported by SNI-CONAHCyT, CATEDRA-CONACYT stimulus No. 71571, and PROFAPI-UAS grant PRO/2022_A7_002. Special thanks to the volunteers, social services, and research residency students who helped with sampling and dissection. This research utilized Soft Matter Interfaces (12-ID) beamline of the National Synchrotron Light Source II, a U.S. Department of Energy (DOE) Office of Science User Facility operated for the DOE Office

of Science by Brookhaven National Laboratory under Contract No. DE-SC0012704. The authors wish to thank Western Sydney University (WSU) Advanced Materials Characterization Facility (AMCF) for access to instrumentation as well as Ken Moran form Moran Scientific Pty ltd for post-processing chemical imaging modifications for our research. The authors would also like to thank the facilities and staff, specifically Dr. Mingjie Xu, at the Irvine Materials Research Institute (IMRI) for their contribution to the collection of electron microscopy data.

Conflict of Interest

The authors declare no conflict of interest.

Data Availability Statement

The data that support the findings of this study are available from the corresponding author upon reasonable request.

Keywords

architected materials, biomineralization, chiton, mechanics, mollusk, self-sharpening

Received: January 27, 2024
Revised: March 12, 2024
Published online:

[1] W. Huang, D. Restrepo, J. Jung, F. Y. Su, Z. Liu, R. O. Ritchie, J. McKittrick, P. Zavattieri, D. Kisailus, *Adv. Mater.* **2019**, *31*, 1901561.
[2] M. A. Meyers, P.-Y. Chen, A. Y.-M. Lin, Y. Seki, *Prog. Mater. Sci.* **2008**, *53*, 1.
[3] S. E. Naleway, M. M. Porter, J. McKittrick, M. A. Meyers, *Adv. Mater.* **2015**, *27*, 5455.
[4] J. C. Weaver, G. W. Milliron, A. Miserez, K. Evans-Lutterodt, S. Herrera, I. Gallana, W. J. Mershon, B. Swanson, P. Zavattieri, E. DiMasi, D. Kisailus, *Science* **2012**, *336*, 1275.
[5] P. van der Wal, H. J. Giesen, J. J. Videler, *Mater. Sci. Eng., C* **1999**, *7*, 129.
[6] J. Rivera, M. S. Hosseini, D. Restrepo, S. Murata, D. Vasile, D. Y. Parkinson, H. S. Barnard, A. Arakaki, P. Zavattieri, D. Kisailus, *Nature* **2020**, *586*, 543.
[7] Z.-Z. Gu, H. Uetsuka, K. Takahashi, R. Nakajima, H. Onishi, A. Fujishima, O. Sato, *Angew. Chem., Int. Ed.* **2003**, *42*, 894.
[8] N. A. Yaraghi, A. A. Trikanad, D. Restrepo, W. Huang, J. Rivera, S. Herrera, M. Zhernenkov, D. Y. Parkinson, R. L. Caldwell, P. D. Zavattieri, D. Kisailus, *Adv. Funct. Mater.* **2019**, *29*.
[9] J. Rivera, S. Murata, M. S. Hosseini, A. A. Trikanad, R. James, A. Pickle, N. Yaraghi, N. Matsumoto, W. Yang, D. Y. Parkinson, H. S. Barnard, P. Zavattieri, A. Arakaki, D. Kisailus, *Adv. Funct. Mater.* **2021**, *31*, 2106468.
[10] H. Aldersey-Williams, *Nat. Mater.* **2004**, *3*, 277.
[11] J. Sedó, J. Saiz-Poseu, F. Busqué, D. Ruiz-Molina, *Adv. Mater.* **2013**, *25*, 653.
[12] A. R. Parker, H. E. Townley, *Nat. Nanotechnol.* **2007**, *2*, 347.
[13] D. Montroni, M. Palanca, K. Morellato, S. Fermani, L. Cristofolini, G. Falini, *Carbohydr. Polym.* **2021**, *251*, 116984.
[14] P. Das, J.-M. Malho, K. Rahimi, F. H. Schacher, B. Wang, D. E. Demco, A. Walther, *Nat. Commun.* **2015**, *6*, 5967.
[15] D. Kisailus, J. H. Choi, J. C. Weaver, W. Yang, D. E. Morse, *Adv. Mater.* **2005**, *17*, 314.
[16] E. A. Zimmermann, B. Gludovatz, E. Schaible, N. K. N. Dave, W. Yang, M. A. Meyers, R. O. Ritchie, *Nat. Commun.* **2013**, *4*, 2634.
[17] Y. Zhang, W. Huang, C. Hayashi, J. Gatesy, J. McKittrick, *J. R. Soc. Interface* **2018**, *15*, 20180093.
[18] W. Huang, N. A. Yaraghi, W. Yang, A. Velazquez-Olivera, Z. Li, R. O. Ritchie, D. Kisailus, S. M. Stover, J. McKittrick, *Acta Biomater.* **2019**, *90*, 267.
[19] K. Tushtev, M. Murck, G. Grathwohl, *Mater. Sci. Eng., C* **2008**, *28*, 1164.
[20] D. Montroni, J. Leonard, M. Rolandi, G. Falini, *J. Struct. Biol.* **2021**, *213*, 107764.
[21] M. E. Launey, M. J. Buehler, R. O. Ritchie, *Annu. Rev. Mater. Res.* **2010**, *40*, 25.
[22] J. C. R. Cardoso, R. C. Félix, V. Ferreira, M. Peng, X. Zhang, D. M. Power, *Sci. Rep.* **2020**, *10*, 7581.
[23] T. Yarra, M. Blaxter, M. S. Clark, *Mol. Biol. Evol.* **2021**, *38*, 4043.
[24] P. Ramos-Silva, D. Wall-Palmer, F. Marlétaz, F. Marin, K. T. C. A. Peijnenburg, *J. Struct. Biol.* **2021**, *213*, 107779.
[25] J. H. E. Cartwright, A. G. Checa, M. J. Vendrasco, *MRS Bull.* **2024**, *49*, 71.
[26] D. Faivre, T. U. Godec, *Angew. Chem., Int. Ed.* **2015**, *54*, 4728.
[27] P. U. P. A. Gilbert, K. D. Bergmann, N. Boekelheide, S. Tambutté, T. Mass, F. Marin, J. F. Adkins, J. Erez, B. Gilbert, V. Knutson, M. Cantine, J. O. Hernández, A. H. Knoll, *Sci. Adv.* **2022**, *8*, eabl9653.
[28] U. G. K. Wegst, H. Bai, E. Saiz, A. P. Tomsia, R. O. Ritchie, *Nat. Mater.* **2015**, *14*, 23.
[29] M. Saunders, C. Kong, J. A. Shaw, D. J. Macey, P. L. Clode, *J. Struct. Biol.* **2009**, *167*, 55.
[30] C. Wang, Q. Y. Li, S. N. Wang, S. X. Qu, X. X. Wang, *Mater. Sci. Eng., C* **2014**, *37*, 1.
[31] J. C. Weaver, Q. Wang, A. Miserez, A. Tantuccio, R. Stromberg, K. N. Bozhilov, P. Maxwell, R. Nay, S. T. Heier, E. DiMasi, D. Kisailus, *Mater. Today* **2010**, *13*, 42.
[32] E. E. de Obaldia, C. Jeong, L. K. Grunenfelder, D. Kisailus, P. Zavattieri, *J. Mech. Behav. Biomed. Mater.* **2015**, *48*, 70.
[33] C. L. Salinas, E. E. de Obaldia, C. Jeong, J. Hernandez, P. Zavattieri, D. Kisailus, *J. Mech. Behav. Biomed. Mater.* **2017**, *76*, 58.
[34] E. Escobar de Obaldia, S. Herrera, L. K. Grunenfelder, D. Kisailus, P. Zavattieri, *J. Mech. Phys. Solids* **2016**, *96*, 511.
[35] F. W. Harrison, A. J. Kohn, *Microscopic Anatomy of Invertebrates, Mollusca One*, *5*, Wiley-Liss, Inc., New York, NY **1994**.
[36] E. Schwabe, *Spixiana* **2010**, *33*, 171.
[37] D. Montroni, X. Zhang, J. Leonard, M. Kaya, C. Amemiya, G. Falini, M. Rolandi, *PLoS One* **2019**, *14*, e0212249.
[38] A. Graham, *J. Zool.* **1973**, *169*, 317.
[39] C. Scheel, S. N. Gorb, M. Glaubrecht, W. Krings, *Biol. Open* **2020**, *9*, 055699.
[40] P. van der Wal, *J. Ultrastruct. Mol. Struct. Res.* **1989**, *102*, 147.
[41] M. Nemoto, Q. Wang, D. Li, S. Pan, T. Matsunaga, D. Kisailus, *Proteomics* **2012**, *12*, 2890.
[42] H. A. Lowenstam, S. Weiner, *Science* **1985**, *227*, 51.
[43] H. A. Lowenstam, *Science* **1967**, *156*, 1373.
[44] A. P. Lee, L. R. Brooker, D. J. Macey, W. van Bronswijk, J. Webb, *Calcif. Tissue Int.* **2000**, *67*, 408.
[45] K.-S. Kim, J. Webb, D. J. Macey, D. D. Cohen, *J. Inorg. Biochem.* **1986**, *28*, 337.
[46] L. A. Evans, D. J. Macey, J. Webb, *Calcif. Tissue Int.* **1992**, *51*, 78.
[47] L. A. Evans, D. J. Macey, J. Webb, *Philos. Trans. R Soc. Lond. B Biol. Sci.* **1990**, *329*, 87.
[48] D. Padilla, *Veliger -Berkeley* **1998**, *41*, 201.
[49] R. S. Steneck, L. Watling, *Mar. Biol.* **1982**, *68*, 299.
[50] J. A. Shaw, D. J. Macey, L. R. Brooker, P. L. Clode, *Biol. Bull.* **2010**, *218*, 132.

[51] J. A. Shaw, D. J. Macey, L. R. Brooker, E. J. Stockdale, M. Saunders, P. L. Clode, *Microsc. Microanal.* **2009**, *15*, 154.
[52] O. H. Avila-Poveda, G. Rodriguez-Dominguez, J. S. Ramirez-Perez, R. Perez-Gonzalez, *J. Molluscan Studies* **2020**, *86*, 72.
[53] O. H. Avila-Poveda, Q. Y. Abadia-Chanona, I. L. Alvarez-Garcia, M. Arellano-Martinez, *J. Molluscan Studies* **2021**, *87*, eyaa033.
[54] B. Ramirez-Santana, *Condicion viscerosomatica, biomineralizacion radular y tipo de alimentacion en Chiton articulatus (Mollusca: Polyplacophora)*, Universidad Autónoma de Sinaloa, Facultad de Ciencias del Mar: Mazatlan, Sinaloa, Mexico, **2021**.
[55] A. Reyes-Gómez, D. Ortigosa, N. Simões, *Zookeys* **2017**, *665*, 1.
[56] A. Reyes-Gómez, Chitons in Mexican waters. Bolletino Malacologico, Societa Italiana di Malacologia Roma, **2003**, 69–82.
[57] R. C. Bullock, *Veliger* **1988**, *31*, 141.
[58] A. J. Ferreira, *Veliger* **1983**, *31*, 141.
[59] O. E. Quiñones, J. Michel-Morfin, *J. Shellfish Res.* **2002**, *21*, 239.
[60] Q. Y. Abadia-Chanona, O. H. Avila-Poveda, M. Arellano-Martinez, B. P. Ceballos-Vazquez, F. Benitez-Villalobos, G. A. Parker, G. Rodriguez-Dominguez, S. Garcia-Ibañez, *Invertebr. Reprod. Dev.* **2018**, *62*, 268.
[61] V. M. V. Arámbula, *AGRICULTURA.- Secretaría de Agricultura y Desarrollo Rural* **2023**.
[62] A. Reyes-Gómez, R. Flores-Garza, L. Galeana-Rebolledo, G. Hernández-Vera, C. M. Galván-Villa, C. Torreblanca-Ramírez, P. Flores-Rodríguez, S. García-Ibañez, E. Ríos-Jara, *Zootaxa* **2022**, *5155*, 451.
[63] M. Prado-Padila, *Variación estacional de la composición de pigmentos fotosintéticos y su importancia en la fisiología del quitón Chiton articulatus (Polyplacophora: Chitonida)*, Universidad Autónoma de Sinaloa, Facultad de Ciencias del Mar: Mazatlan, Sinaloa, Mexico, **2023**.
[64] A. Pohl, S. A. Herrera, D. Restrepo, R. Negishi, J.-Y. Jung, C. Salinas, R. Wuhrer, T. Yoshino, J. McKittrick, A. Arakaki, M. Nemoto, P. Zavattieri, D. Kisailus, *J. Mech. Behav. Biomed. Mater.* **2020**, *111*, 103991.
[65] J.-E. Lee, J. Connolly, W. Yang, G. Freychet, T. Wang, S. A. Herrera, S. Murata, P. S. Dasika, D. Montroni, A. Pohl, C. Zhu, M. Zhernenkov, R. Wuhrer, L. Sheppard, M. Nemoto, A. Arakaki, P. Zavattieri, D. Kisailus, *J. Compos. Mater.* **2023**, *57*, 565.
[66] D. Wallis, J. Harris, C. F. Böhm, D. Wang, P. Zavattieri, P. Feldner, B. Merle, V. Pipich, K. Hurle, S. Leupold, L. N. Hansen, F. Marin, S. E. Wolf, *Mater. Adv.* **2022**, *3*, 1527.
[67] Z.-Z. Du, *eXtended Finite Element Method (XFEM) in Abaqus*, Johnston, RI, **2009**.
[68] A. Pohl, S. A. Herrera, D. Restrepo, R. Negishi, J.-Y. Jung, C. Salinas, R. Wuhrer, T. Yoshino, J. McKittrick, A. Arakaki, M. Nemoto, P. Zavattieri, D. Kisailus, *J. Mech. Behav. Biomed. Mater.* **2020**, *111*, 103991.
[69] Q. Wang, M. Nemoto, D. Li, J. C. Weaver, B. Weden, J. Stegemeier, K. N. Bozhilov, L. R. Wood, G. W. Milliron, C. S. Kim, E. Dimasi, D. Kisailus, *Adv. Funct. Mater.* **2013**, *23*, 2908.
[70] L. K. Grunenfelder, E. E. De Obaldia, Q. Wang, D. Li, B. Weden, C. Salinas, R. Wuhrer, P. Zavattieri, D. Kisailus, *Adv. Funct. Mater.* **2014**, *24*, 6093.
[71] H. D. Espinosa, A. Zaheri, H. Nguyen, D. Restrepo, M. Daly, M. Frank, J. McKittrick, *Matter* **2019**, *1*, 1246.
[72] S. Bentov, C. Brownlee, J. Erez, *Proc. Natl. Acad. Sci. USA* **2009**, *106*, 21500.
[73] L. M. Gordon, D. Joester, *Nature* **2011**, *469*, 194.
[74] A. Bigi, G. Falini, E. Foresti, A. Ripamonti, M. Gazzano, N. Roveri, *J. Inorg. Biochem.* **1993**, *49*, 69.
[75] D. Laurencin, N. Almora-Barrios, N. H. de Leeuw, C. Gervais, C. Bonhomme, F. Mauri, W. Chrzanowski, J. C. Knowles, R. J. Newport, A. Wong, Z. Gan, M. E. Smith, *Biomaterials* **2011**, *32*, 1826.
[76] D. Montroni, F. Sparla, S. Fermani, G. Falini, *Acta Biomater.* **2021**, *120*, 81.
[77] T. Wang, W. Huang, C. H. Pham, S. Murata, S. Herrera, N. D. Kirchhofer, B. Arkook, D. Stekovic, M. E. Itkis, N. Goldman, L. Zepeda-Ruiz, G. Freychet, M. Zhernenkov, M. Nemoto, A. Arakaki, D. Kisailus, *Small Struct.* **2022**, *3*, 2100202.
[78] W. Huang, M. Shishehbor, N. Guarín-Zapata, N. D. Kirchhofer, J. Li, L. Cruz, T. Wang, S. Bhowmick, D. Stauffer, P. Manimunda, K. N. Bozhilov, R. Caldwell, P. Zavattieri, D. Kisailus, *Nat. Mater.* **2020**, *19*, 1236.
[79] M. Y. He, A. G. Evans, J. W. Hutchinson, *Int. J. Solids Struct.* **1994**, *31*, 3443.
[80] E. Beniash, C. A. Stifler, C.-Y. Sun, G. S. Jung, Z. Qin, M. J. Buehler, P. U. P. A. Gilbert, *Nat. Commun.* **2019**, *10*, 4383.
[81] H. A. Lowenstam, *Science* **1967**, *156*, 1373.
[82] R. J. Wealthall, L. R. Brooker, D. J. Macey, B. J. Griffin, *J. Morphol.* **2005**, *265*, 165.
[83] D. Montroni, *Hierarchically organized chitin-based matrices, Dissertation*, University of Bologna, AMS Dottorato **2020**.
[84] W. Huang, D. Montroni, T. Wang, S. Murata, A. Arakaki, M. Nemoto, D. Kisailus, *Acc. Chem. Res.* **2022**, *55*, 1360.
[85] M. Y. He, A. G. Evans, J. W. Hutchinson, *Int. J. Solids Struct.* **1994**, *31*, 3443.
[86] R. Wuhrer, K. Moran, *IOP Conf. Ser. Mater. Sci. Eng.* **2016**, *109*, 012019.
[87] R. Wuhrer, K. Moran, *Microsc. Microanal.* **2015**, *21*, 2191.
[88] K. Moran, R. Wuhrer, *Microchim. Acta* **2006**, *155*, 59.
[89] W. C. Oliver, G. M. Pharr, *J. Mater. Res.* **2004**, *19*, 3.